Impact of a Mean Current on the Internal Tide Energy Dissipation at the Critical Latitude

O. RICHET, C. MULLER,[a] AND J.-M. CHOMAZ

LadHyX, Ecole Polytechnique, Palaiseau, France

(Manuscript received 24 August 2016, in final form 12 January 2017)

ABSTRACT

Previous numerical studies of the dissipation of internal tides in idealized settings suggest the existence of a critical latitude (~29°) where dissipation is enhanced. But observations only indicate a modest enhancement at this latitude. To resolve this difference between observational and numerical results, the authors study the latitudinal dependence of internal tides' dissipation in more realistic conditions. In particular, the ocean is not a quiescent medium; the presence of large-scale currents or mesoscale eddies can impact the propagation and dissipation of internal tides. This paper investigates the impact of a weak background mean current in numerical simulations. The authors focus on the local dissipation of high spatial mode internal waves near their generation site. The vertical profile of dissipation and its variation with latitude without the mean current are consistent with earlier studies. But adding a weak mean current has a major impact on the latitudinal distribution of dissipation. The peak at the critical latitude disappears, and the dissipation is closer to a constant, albeit with two weak peaks at ~25° and ~35° latitude. This disappearance results from the Doppler shift of the internal tides' frequency, which hinders the nonlinear transfer of energy to small-scale secondary waves via the parametric subharmonic instability (PSI). The new two weak peaks correspond to the Doppler-shifted critical latitudes of the left- and right-propagating waves. The results are confirmed in simulations with simple sinusoidal topography. Thus, although nonlinear transfers via PSI are efficient at dissipating internal tides, the exact location of the dissipation is sensitive to large-scale oceanic conditions.

1. Introduction

In the abyssal ocean, away from boundaries where exchanges with the atmosphere or land can occur, the largest buoyancy forcing happens via mixing. In the ocean interior, observations indicate that diapycnal mixing (mixing across isopycnals) is largely dominated by the breaking of internal waves (Polzin et al. 1997; Ledwell et al. 2000; Waterhouse et al. 2014). Internal waves are ubiquitous in the ocean (Garrett and Munk 1979). They transport energy, and when they become unstable and break, they dissipate this energy, thereby contributing to mixing oceanic water masses. This mixing is strongly inhomogeneous in space and time, but its distribution remains poorly understood. Uncertainties in the spatial distribution of wave energy dissipation and concomitant diapycnal mixing limit our ability to understand the ocean global circulation and water mass formation, especially deep waters whose isopycnals do not outcrop at high latitudes (Talley 2013; Ferrari 2014).

Numerous studies show the impact of inhomogeneous mixing on the abyssal circulation from idealized models (Samelson 1998; Nikurashin et al. 2012; Mashayek et al. 2015) to more realistic global ocean models (Jayne 2009; Munday et al. 2011; Melet et al. 2016). Global climate models do not resolve processes associated with internal waves, which are therefore parameterized. The consumption of Antarctic Bottom Water (AABW; dense cold bottom water mass formed in Antarctica) in the ocean interior is strongly influenced by wave-induced diapycnal mixing (Talley 2013; Melet et al. 2016). It is primarily influenced by internal tides (Nikurashin and Ferrari 2013; De Lavergne et al. 2016a,b), which are internal waves generated by barotropic tidal currents flowing above topography [see Garrett and Kunze (2007) for a review]. Depending on the spatial distribution of internal tides' dissipation and the induced mixing, estimates of AABW upwelling differ by a factor of 2 or more (De Lavergne et al. 2016a).

[a] Current affiliation: Laboratoire de Météorologie Dynamique, Ecole Normale Supérieure, Paris, France.

Corresponding author: O. Richet, oceane.richet@ladhyx.polytechnique.fr

DOI: 10.1175/JPO-D-16-0197.1

One major uncertainty is the vertical profile of the internal tides' dissipation. To leading order, its maximum height, which determines the depth of the AABW return flow to the Southern Ocean along isopycnals (Ferrari 2014), is dictated by the topographic height (Nikurashin and Ferrari 2013), since dissipation is strongly localized near topography. Nevertheless, vertical profiles with enhanced dissipation up to 500 m or 1 km above topography have been found in numerical studies (Nikurashin and Legg 2011). Along with the Antarctic latitudinal extent of ice cover, the height of dissipation dictates exchanges with the atmosphere (carbon dioxide, oxygen, etc.) in the Southern Ocean and hence largely determines the carbon storage in the deep ocean (Ferrari et al. 2014). Another major uncertainty is the fraction of internal tide energy that dissipates locally near the seafloor upon generation and the remaining fraction of internal tides that escape and are hence available to dissipate remotely. The latter could contribute as low as 1 Sv (1 Sv = $10^6\,m^3\,s^{-1}$) and as high as 28 Sv of AABW upwelling depending on their energy and vertical dissipation profile (De Lavergne et al. 2016a). Understanding internal tides' sources, mechanisms of energy transfers, and the resulting mixing is therefore a crucial step to understand the global distribution of temperature, salinity, and biogeochemical tracers in the abyssal ocean and to improve the representation of wave-induced mixing in climate models.

Mechanisms of internal tides breaking are not well understood, and several mechanisms have been proposed. These include breaking through convective or shear instability (Muller and Bühler 2009), scattering by the bottom (Müller and Xu 1992) and the thermocline (Gerkema 2001), critical reflection (Gemmrich and Klymak 2015), scattering by mesoscale features (Rainville and Pinkel 2006), or energy transfer to smaller scales via nonlinear wave–wave interactions (Polzin 2009; MacKinnon and Winters 2005). It is believed that internal tides with small scales (high spatial modes, generated by topography with horizontal scales below 10 km or so) are dissipated near their generation site (St. Laurent and Garrett 2002; Muller and Bühler 2009; Lefauve et al. 2015), while waves with larger scales (low spatial modes) generated at large topographic features (e.g., the Hawaiian Ridge) can propagate thousands of kilometers across oceanic basins (Hazewinkel and Winters 2011). We focus on the local dissipation of internal tides near their generation site. Of particular interest is the latitudinal distribution of the local dissipation (high-mode internal tides).

Recent idealized simulations show that the latitudinal distribution of tidal mixing may be largely determined by an instability known as the parametric subharmonic instability (PSI). PSI is the class of resonant wave–wave nonlinear interactions wherein energy is transferred from large scales to smaller scales and where the frequencies of the secondary waves are near half the primary frequency (Bouruet-Aubertot et al. 1995; Staquet and Sommeria 2002; Bourget et al. 2013). When the primary waves are internal tides generated at the tidal frequency ω_0 (about twice a day for the largest semidiurnal lunar tide), PSI yields two secondary waves through nonlinear interactions with frequency $\omega_0/2$. Both idealized numerical studies of low (MacKinnon and Winters 2005) and high (Nikurashin and Legg 2011) modes find a large enhancement of the dissipation of internal tides at a critical latitude of ~29° ($f = 0.7 \times 10^{-4}\,s^{-1}$). This corresponds to the latitude where the frequency of the secondary waves $\omega_0/2$ matches the Coriolis frequency $f = 2\Omega \sin\phi$, where Ω denotes Earth's rotation rate and ϕ denotes latitude. In other words, the secondary waves at the critical latitude are near-inertial waves. The secondary waves have frequencies lower than the primary waves and hence smaller scales.

On the other hand, observations only indicate a modest enhancement of dissipation at the critical latitude (Alford et al. 2007; MacKinnon et al. 2013), at least for low-mode internal tides. Indeed these observations were not deep enough to capture the high modes discussed in Nikurashin and Legg (2011). In other words, observations of low modes do not confirm the "catastrophic" dissipation that numerical studies of low modes (MacKinnon and Winters 2005) and high modes (Nikurashin and Legg 2011) suggest. For the low-mode internal tides propagating away from their generation site, it was suggested that the time scale of PSI may be too slow to significantly impact the propagating low-mode wave packet as it crosses the critical latitude (Hazewinkel and Winters 2011). But for the high-mode internal tides whose group velocities are smaller and who are continuously generated near the seafloor, PSI could significantly impact their local dissipation. This is the question addressed here, namely, what role does PSI play in the local dissipation of internal tides near their generation site? In particular, do we expect the enhanced dissipation at the critical latitude observed in the idealized simulations of Nikurashin and Legg (2011) under more realistic oceanic conditions?

To address these questions, we investigate whether the presence of a background mean current can impact the enhanced local dissipation at the critical latitude. Indeed, internal tides do not propagate through a quiescent ocean. Large-scale currents or mesoscale eddies are ubiquitous in the ocean and can yield currents with amplitudes comparable to or larger than the barotropic tide (Nikurashin and Ferrari 2011). This mean current

can interact with internal tides and modify their propagation and dissipation. In this paper, we investigate the impact of a weak mean current, with an amplitude on the order of the barotropic tide, on the high-mode internal tides' dissipation.

Section 2 describes the numerical model used and the setting. Section 3 presents results first without a mean current, reproducing the main results of Nikurashin and Legg (2011) and second with a mean current whose impact is discussed. In section 4, we validate the hypothesis of a Doppler effect with idealized simulations of internal tides generated by simple monochromatic sinusoidal topography. Conclusions and implications for the large-scale circulation are discussed in section 5.

2. Methods

a. Numerical model

Our goal is to investigate the impact of a mean current on the resonant dissipation found at the critical latitude in the simulations of Nikurashin and Legg (2011). We therefore follow their methodology and use the same numerical model in similar settings. Namely, we use the Massachusetts Institute of Technology General Circulation Model (MITgcm; Marshall et al. 1997), a high-resolution numerical model in nonhydrostatic configuration. The nonhydrostatic configuration allows the explicit representation of processes such as hydraulic jumps or Kelvin–Helmholtz instabilities. The MITgcm solves the equations of an incompressible fluid under the Boussinesq approximation. The model is developed with the finite-volume techniques to provide the treatment of irregular geometries like the topography using the MITgcm partial cells' architecture. The bottom boundary is treated with a no-slip condition.

The main characteristics of the domain are synthesized in Fig. 1. The domain is two-dimensional with horizontal periodicity in the x direction. The horizontal size of the domain is 60 km with a uniform resolution of $\Delta x = 30$ m, and the total vertical extent is 7.5 km. The 4.5-km bottom layer has a uniform resolution of $\Delta z = 10$ m. The last upper 3 km form the sponge layer where the resolution is progressively stretched from $\Delta z = 10$ to 70 m. The model time step is 30 s. Although two-dimensional ($\partial/\partial y \equiv 0$), we allow for a velocity v constant in the y direction. As in Nikurashin and Legg (2011), these high-resolution idealized simulations are designed to allow the resolution of a wide range of spatial and temporal scales of the turbulence.

We are interested in the local dissipation of internal tides near their generation site, so we neglect reflection at the ocean surface and assume a semi-infinite ocean.

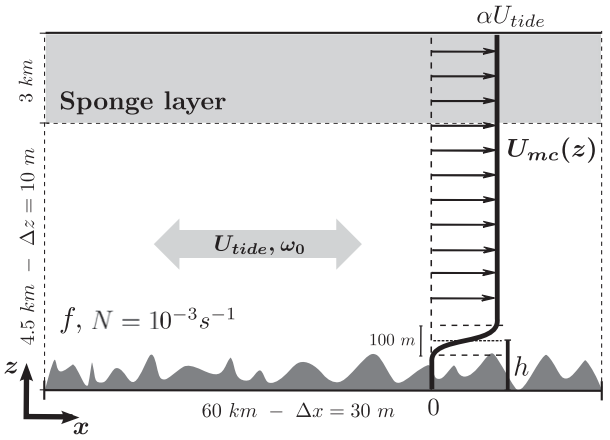

FIG. 1. Schematic of the numerical setup. The barotropic tidal current, with amplitude U_{tide} and frequency ω_0, interacts with a one-dimensional realistic topography in a stratified (N constant) and rotating (f varying with latitude) fluid. The mean flow U_{mc} has an amplitude equal to zero below the maximum of topography and reaches an amplitude αU_{tide} 100 m above the maximum of topography. The parameter α governing the relative strength of the mean current varies between 0 and 1 in the various simulations. The gray, shaded layer at the top of the domain corresponds to the sponge layer.

We therefore add the sponge layer at the top of the domain to absorb the upward-propagating waves, which do not dissipate locally and whose remote dissipation would require further investigation beyond the scope of this study. In the sponge layer, buoyancy and momentum are damped with a linear drag with a time scale of 1 h.

b. Settings

In the simulations, the fluid is linearly stratified in the vertical with constant buoyancy frequency $N = 10^{-3}\,\text{s}^{-1}$ representative of the deep-ocean stratification. The Coriolis frequency is varied with varying latitude to investigate the latitudinal variation of internal tides' dissipation. At the critical latitude 28.8°, $f = 0.7 \times 10^{-4}\,\text{s}^{-1}$. The horizontal and vertical viscosities and diffusivities are set to $\nu_h = \nu_v = 2 \times 10^{-3}\,\text{m}^2\,\text{s}^{-1}$ and $\kappa_h = \kappa_v = 10^{-4}\,\text{m}^2\,\text{s}^{-1}$ [values close to the ones used in Nikurashin and Legg (2011), who found that the energy dissipation profiles are robust to reasonable changes of these values]. All simulations are initiated from a state at rest and run for 30 days (a statistically steady state is reached in 5 to 10 days depending on the simulation).

c. Topography

Following Nikurashin and Legg (2011), we focus on tidal generation in the Brazil Basin where high levels of mixing have been observed (Polzin et al. 1997; Waterhouse et al. 2014) and are attributed to internal

tides breaking. In the Brazil Basin, the Mid-Atlantic Ridge (MAR) is almost oriented east–west. Abyssal ridges are anisotropic and elongated perpendicular to the direction of spreading. For this reason, and in the case of the MAR, the roughest topography is oriented almost south–north, and a 2D numerical model in this direction is a good first approximation for wave generation. Topographic variability associated with abyssal hills is described by a one-dimensional topography spectrum obtained by integrating the two-dimensional spectrum of Goff and Jordan (1989; see also Goff and Arbic 2010),

$$H(k,l) = \frac{4\pi\nu h^2}{k_0 l_0}\left(\frac{k^2}{k_0^2}+\frac{l^2}{l_0^2}+1\right)^{-(\nu+1)}, \qquad (1)$$

along the smooth direction [see Muller and Bühler (2009) and Nikurashin and Legg (2011) for more details about the one-dimensional topography computation]. The topography used in section 3 is designed to have this observed spectrum with parameters from the Brazil Basin: root-mean-square (rms) height $h = 110\,\mathrm{m}$, high-wavenumber slope $\nu = 0.90$, and rolloff wavenumber $k_0 = 1.0 \times 10^{-3}\,\mathrm{m}^{-1}$.

In section 4, additional simulations with idealized sinusoidal topography will be performed. The sinusoidal topography is designed to have similar vertical and horizontal Froude numbers as the realistic topography, $\mathrm{Fr}_\nu = U_{\mathrm{tide}}/Nh \approx 10^{-1}$ and $\mathrm{Fr}_h = U_{\mathrm{tide}}/(N2\pi/k_0) \approx 4\times10^{-3}$, respectively, where U_{tide} denotes the amplitude of the barotropic tide (see next section for more details). This ensures that we keep the same flow regimes. We note in passing that holding Fr_h and Fr_ν constant implies that both the ratio of the wave slope to topography slope $\approx (\omega/N)/[h/(2\pi/k)]$ and the tidal excursion $(U/\omega)/(2\pi/k)$ are kept constant, since ω and N are the same in all simulations. Hence, the rms height of the sinusoidal topography is set to $h = 110\,\mathrm{m}$, and the horizontal wavenumber is equal to $k_0 \approx 0.8 \times 10^{-3}\,\mathrm{m}^{-1}$.

d. Tidal and mean currents imposed

The tidal barotropic flow is forced by adding a body force to the momentum equations, yielding a barotropic semidiurnal lunar M_2 tide $U(t) = U_{\mathrm{tide}}\sin(\omega_0 t)$ with amplitude $U_{\mathrm{tide}} = 2.5\,\mathrm{cm\,s}^{-1}$ and frequency $\omega_0 = 1.4 \times 10^{-4}\,\mathrm{s}^{-1}$. In some of the simulations, a mean current U_{mc} is also imposed. To allow waves to feedback on the mean current, we do not use relaxation toward an imposed profile but instead we impose a geostrophic current by adding a meridional pressure gradient. Our goal is to investigate the impact of this mean current on the propagation of waves, not on their generation. We therefore only add the mean current above topography and increase the amplitude of U_{mc} from 0 at the maximum height of topography to αU_{tide} a hundred meters above that height using a smooth arctan profile (see the appendix for more details about the few lee waves generated by the mean current intersecting the highest topographic features and the negligible energy dissipation associated with those). The parameter α is varied between 0 and 1 in the different simulations to assess the impact of the relative amplitude of the mean current on the internal tides. The vertical profile of the mean current U_{mc} is shown in Fig. 1.

As noted above, our goal is to investigate the impact of the mean current on the internal tides and their energy dissipation to secondary waves via PSI. We therefore need to make sure that the 100-m vertical shear layer does not significantly impact the upward-propagating internal tides before they reach the mean current region. Two possible undesirable effects of the shear layer can destabilize the primary waves and prevent their upward propagation: shear instability and/or a critical layer. Empirically, we will see that the energy dissipation is not enhanced in the shear layer, implying that the waves can propagate through and past the shear layer.

This is expected theoretically since shear instability is determined by the nondimensional Richardson number $\mathrm{Ri} = N^2/(\partial u/\partial z)^2 \geq 4$ for a 100-m-thick shear layer and $0 \leq \alpha \leq 1$ (strength of the mean current). Hence, $\mathrm{Ri} > 1/4$, ensuring stability in the shear layer. The second possible sources of dissipation are critical levels, where the mean current matches the horizontal phase speed $c = \omega_0/k$ of the internal tides (Booker and Bretherton 1967; Maslowe 1986). At critical levels, the momentum of the waves is transferred to the mean flow, and the waves are attenuated. The nondimensional parameter relevant in that case is $U/c = Uk/\omega_0$, which is the so-called tidal excursion (Garrett and Kunze 2007), typically below unity in the ocean. In our simulations $U/c = O(10^{-1})$, ensuring stability through the shear layer. We therefore expect the internal tides generated at the topography to propagate upward past the shear layer into the mean current region $U \equiv U_{\mathrm{mc}}$ of interest.

3. Results: Realistic topography

In this section, we investigate the dissipation of internal tides generated by realistic topography, without and with mean current. We start by reproducing the peak of tidal dissipation at the critical latitude found by Nikurashin and Legg (2011; our control simulations). In these control simulations, the only forcing is the barotropic tide. We then add a mean current and investigate whether the enhanced dissipation at the critical latitude is robust or altered.

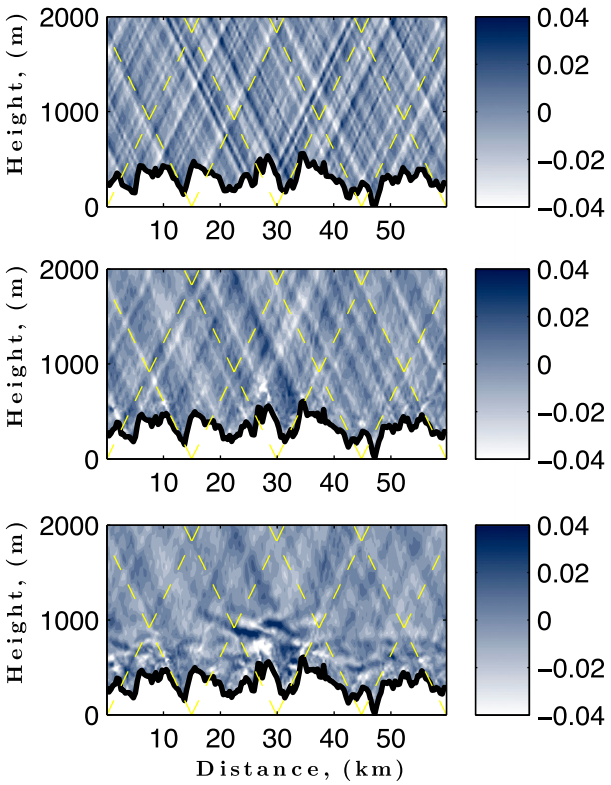

FIG. 2. Snapshots of the wave zonal velocity ($m\,s^{-1}$) from the control simulation without mean current at the critical latitude ($f = 0.7 \times 10^{-4}\,s^{-1}$, $\alpha = 0$) after 5 (middle) and (bottom) 19 days of simulation. (top) The linear solution is also shown for comparison as well as wave characteristics from the linear theory dispersion relation (dashed yellow lines).

a. *Control case: Tidal energy transfer without mean current*

Figure 2 shows snapshots of the zonal velocity anomaly (deviation from the zonally averaged flow) at 5 and 19 days in the control simulation at the critical latitude ($f = 0.7 \times 10^{-4}\,s^{-1}$, $\alpha = 0$). In the simulations, internal tides are generated at the topography as the barotropic tide oscillates back and forth. As these waves propagate into the ocean interior, they either break and dissipate or propagate all the way to 4.5 km, above which they are absorbed in the sponge layer. Internal tides typically take 5–10 days to reach the sponge layer (depending on their scales, larger scales propagate faster). This time corresponds to the establishment of a stationary wave field in the ocean interior, where the energy input from the barotropic tide is equilibrated by the energy output into wave dissipation in the ocean interior or wave damping in the sponge layer.

At day 5, the generation of internal tides is in good agreement with linear theory, shown in the top panel (Bell 1975; Muller and Bühler 2009). The dashed yellow lines repeated in all the panels indicate the linear wave slopes $k/m = \pm\sqrt{(\omega_0^2 - f^2)/(N^2 - \omega_0^2)}$. The observed wave field is the multichromatic superposition of plane waves generated at the various wavelengths of the topography spectrum. Note that from their dispersion relationship, internal waves propagate with a slope determined solely by their temporal frequency ω_0 for waves generated at the fundamental tidal frequency, which clearly dominate the wave field here (we can also observe some higher harmonics with frequency $2\omega_0$ and accordingly steeper slopes).

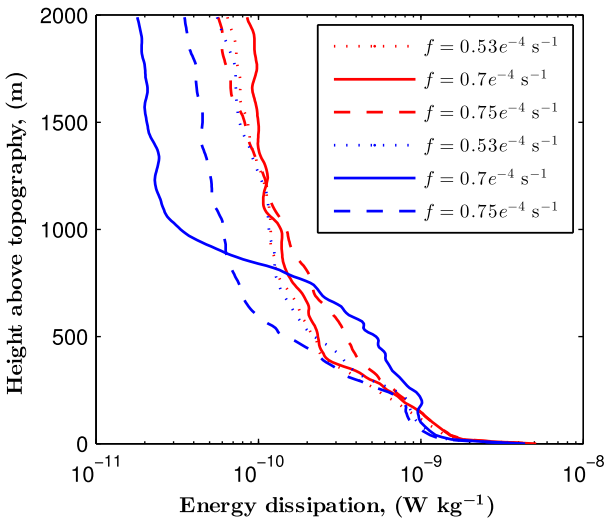

FIG. 3. Profiles of energy dissipation rates averaged zonally and over the last 10 days of the simulations. Blue profiles correspond to simulations with $\alpha = 0$ (no mean current), and red profiles correspond to simulations with $\alpha = 1$ (mean current).

After 19 days, the wave field has largely diverged from linear theory, and horizontal waves appear. This is consistent with the results of Nikurashin and Legg (2011), who show that nonlinear interactions spontaneously generate secondary waves at $\omega_0/2$, which is equal to f at the critical latitude. The horizontal waves observed toward the end of the simulation in Fig. 2 are those secondary near-inertial waves. They largely dominate the wave field at day 19, consistent with earlier results in the literature that the transfer of energy from the primary wave at ω_0 to secondary waves at $\omega_0/2$ is maximum when there is resonance with $f = \omega_0/2$, that is, at the critical latitude.

The energy dissipation rate diagnosed from the control simulation is shown in Fig. 3 (blue plain curve) and compared to dissipation rate at other latitudes (blue dashed and dotted curves). The dissipation rate is computed as

$$\varepsilon = \nu_i \left\langle \left(\frac{\partial u_j}{\partial x_i}\right)\left(\frac{\partial u_j}{\partial x_i}\right)\right\rangle, \qquad (2)$$

where ν is viscosity, u is velocity, $\langle . \rangle$ denotes zonal and temporal mean, and repeated indices are understood as sums. The dissipation rate is averaged over the last 10 days of simulation. The vertical dissipation profiles obtained at different latitudes (solid line $f = 0.7 \times 10^{-4}\,\mathrm{s}^{-1}$, dotted line $f = 0.53 \times 10^{-4}\,\mathrm{s}^{-1}$, and dashed line $f = 0.75 \times 10^{-4}\,\mathrm{s}^{-1}$) exhibit three distinct regions. The first one extends a few tens of meters above topography, where, for all latitudes, the energy dissipation is enhanced up to $O(10^{-8})\,\mathrm{W\,kg}^{-1}$. This region corresponds to the bottom boundary layer where energy dissipation is sustained by nonlinear effects such as flow separation from topography, hydraulic jumps, and direct breaking of the smallest-scale internal tide $O(50)$ m or less (not shown). The second one is the region above the bottom boundary layer until the first kilometer above topography. In this region, the energy dissipation profile at the critical latitude ($f = 0.7 \times 10^{-4}\,\mathrm{s}^{-1}$) is different from those obtained at the other latitudes ($f = 0.53 \times 10^{-4}\,\mathrm{s}^{-1}$ and $f = 0.75 \times 10^{-4}\,\mathrm{s}^{-1}$), with a 1-km-thick "pocket" of enhanced dissipation. Dissipation is enhanced up to $O(10^{-9})\,\mathrm{W\,kg}^{-1}$ at a height of 500 m above topography. This is consistent with Fig. 2; at the critical latitude tidal energy is transferred efficiently to near-inertial frequencies via PSI, while at the other latitudes the instability is not as efficient at transferring energy to near-inertial waves. The third and last region is higher than 1 km above topography. The energy dissipation is close to the background value of $O(10^{-10})\,\mathrm{W\,kg}^{-1}$, except at the critical latitude where the energy dissipation falls to $O(10^{-11})\,\mathrm{W\,kg}^{-1}$, as in Nikurashin and Legg (2011).

The vertically integrated energy dissipation over the bottom 50 m, and from 50 m to 2 km above topography, is shown for several latitudes in Fig. 4 (blue curves). Consistent with the above results and earlier studies, the bottom energy dissipation (50 m from topography) is largely insensitive to f, while the energy dissipation above the bottom boundary layer is strongly dependent on the Coriolis frequency. It increases from near the equator ($f = 0.2 \times 10^{-4}\,\mathrm{s}^{-1} \Rightarrow \varepsilon \approx 0.3\,\mathrm{mW\,m}^{-2}$) to the critical latitude ($f = 0.7 \times 10^{-4}\,\mathrm{s}^{-1} \Rightarrow \varepsilon \approx 0.6\,\mathrm{mW\,m}^{-2}$) and decreases rapidly poleward ($f = 1 \times 10^{-4}\,\mathrm{s}^{-1} \Rightarrow \varepsilon \approx 0.2\,\mathrm{mW\,m}^{-2}$). The energy flux at the topography, defined as the vertical wave energy flux $p'w'$ averaged over the surface bounding the topography

$$\mathrm{EF} = \left\langle \int p'w'\,dxdy \Big/ \left(\int dxdy \right) \right\rangle_T, \qquad (3)$$

where p' and w' are pressure and vertical velocity zonal anomalies and $\langle . \rangle_T$ denotes the time average between 5th and 15th tidal periods, is shown in the middle panel

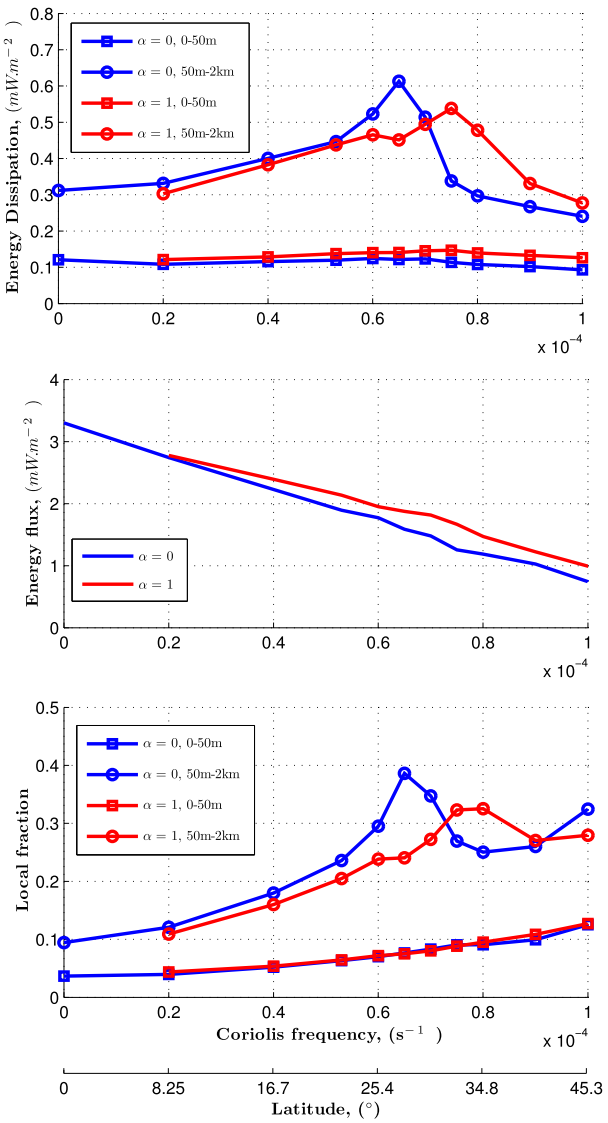

FIG. 4. (top) Energy dissipation rate integrated in the bottom 50 m (squares) and between 50 and 2 km (circles). (middle) Energy flux at the topography. (bottom) Energy dissipation expressed as a fraction of the energy flux at the topography. Blue curves correspond to simulations without mean current ($\alpha = 0$), and red curves correspond to simulations with mean current ($\alpha = 1$; note that in that case $f = 0$ is not shown since a mean current cannot be imposed via geostrophy with $f = 0$; see section 2 for details).

in Fig. 4. It decreases with latitude [consistent with the linear theory, which predicts $\mathrm{EF} \propto \sqrt{\omega_0^2 - f^2}$ decaying with f (Muller and Bühler 2009)]. The local dissipation fraction, shown in the bottom panel in Fig. 4 and defined as the energy dissipation vertically integrated normalized by the energy flux at the topography, increases from 10% at the equator (latitude 0°) to 40% at the critical latitude (28.8°) and decreases to 25%–30% at higher latitudes. In other words, our simulations so far confirm

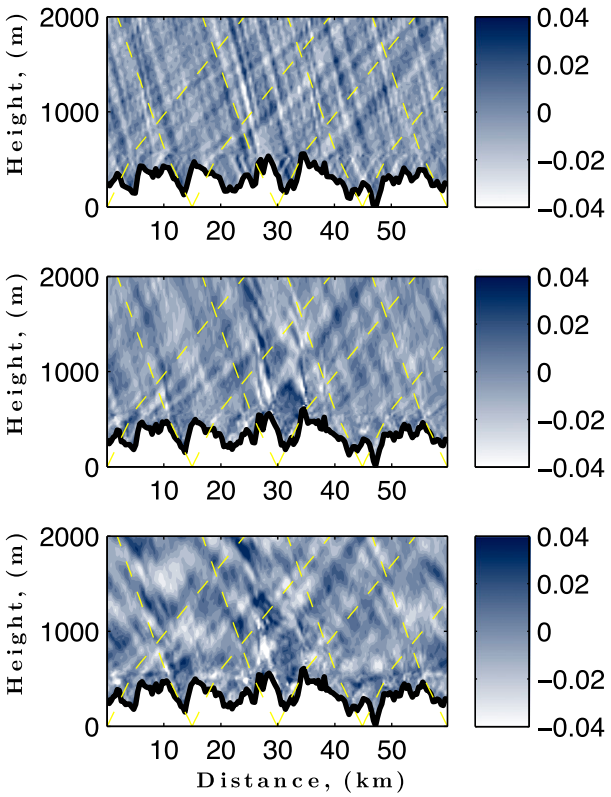

FIG. 5. Snapshots of the wave zonal velocity ($m\,s^{-1}$) from the simulation with a mean current ($f = 0.7 \times 10^{-4}\,s^{-1}$, $\alpha = 1$) after (middle) 5 and (bottom) 19 days of simulation. (top) The linear solution is also shown for comparison with the slopes (yellow dashed lines) from linear theory with Doppler shift (computed using a typical topographic wavenumber close to the topography spectrum wavenumber rolloff k_0).

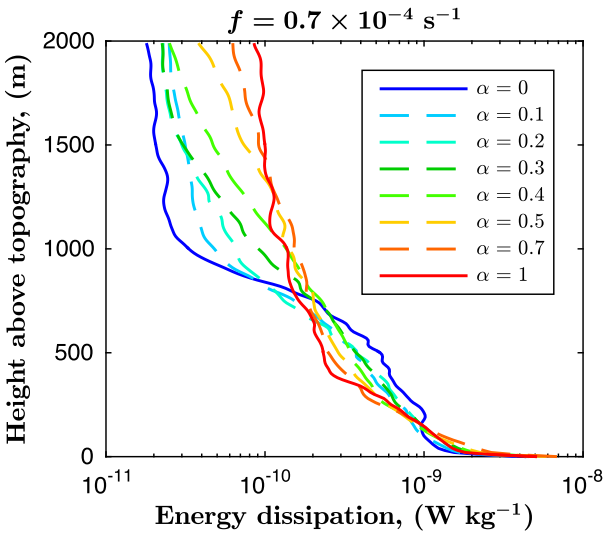

FIG. 6. Profiles of energy dissipation rates averaged zonally and over the last 10 days of the simulations. Each profile corresponds to a simulation with a given α (which dictates the strength of the mean current) at $f = 0.7 \times 10^{-4}\,s^{-1}$.

the results from earlier studies that the critical latitude may serve as a "hot spot" for tidal dissipation.

b. *Impact of a mean current on energy dissipation*

We now investigate the impact of a mean current on the radiation and breaking of internal tides. As noted in section 2, the mean current increases progressively above the topography to reach an amplitude of αU_{tide} a hundred meters above the topography, so that the generation of internal tides is unchanged (see Fig. 1 and appendix for details).

The zonal wave field (deviation from the zonally averaged flow) at the critical latitude is shown in Fig. 5 after 5 (middle) and 19 (bottom) days of simulation. Comparing Figs. 2 and 5, a striking feature is the absence of the near-inertial horizontal waves that developed at day 19 near the seafloor in Fig. 2. Without a mean current, the linear wave field was largely distorted by nonlinearities, yielding strong near-inertial waves at day 19. This is not the case in Fig. 5 once a mean current is added; here instead the middle and bottom panels of Fig. 5 are similar. As before, we added the linear wave slopes; note, however, that the Doppler shift $\omega_0 - U_{\text{mc}}k$, and hence the wave slope, is scale dependent. For illustration purposes we picked $k = k_0$, the rolloff wavenumber in the spectrum, for the yellow lines, showing reasonable but not perfect (as expected) agreement with the linear theory (top panel). Overall, the wave field remains fairly close to the linear wave field (top panel) even after 19 days. So the mean current seems to impact the nonlinear transfer of energy to secondary near-inertial waves.

We further quantify this observed reduction of nonlinear secondary wave generation by looking at energy dissipation profiles in Fig. 6. Each profile corresponds to a simulation where α is fixed. In the boundary layer (tens of meters from topography), the energy dissipation is not affected by the mean current (this is unsurprising since the mean current starts above topography). Above the bottom boundary layer, when α is increased, the enhanced energy dissipation associated with PSI at the critical latitude progressively disappears. Going back to the vertical profiles of dissipation (Fig. 3), we superimpose the new profiles obtained with a mean current ($\alpha = 1$, red curves) to the previous profiles (blue curves). The new profiles at all latitudes almost perfectly match earlier profiles at nonresonant latitudes. Thus, the latitude dependence of energy dissipation seems to disappear when a mean current is added.

This result is also visible on vertically integrated energy dissipation rates (Fig. 4, red curve). The energy

dissipation in the boundary layer is unchanged when the mean current is added. But in the ocean interior, the enhancement of dissipation is weaker and more spread out for values of f between 0.6×10^{-4} and $0.85 \times 10^{-4}\,\mathrm{s}^{-1}$ (latitudes between 20° and 35°). The energy flux at the topography is shown in the middle panel in Fig. 4 and is quite similar to simulations without a mean current, showing that the mean current does not affect the generation of waves. The local dissipation fraction (bottom panel Fig. 4) increases slowly from 10% at the equator to ~33% at 35° latitude and decreases at higher latitudes. Overall, with a mean current, the energy dissipation fraction is less peaked and closer to a constant northward of 25° latitude. Closer inspection of the local fraction shows that there are still two weak ''resonant'' latitudes shifted to ~25° and ~35° latitudes. To understand this behavior and the physical processes responsible for the new latitudinal dependence of dissipation, we analyze the kinetic energy spectrum.

c. *Kinetic energy spectrum and Doppler effects*

Given that the mean current is above the topography and thus does not impact the generation of waves, the picture that emerges is that the mean current impacts the propagation of the waves and, more precisely, the generation of secondary waves via PSI. One possible explanation is that the growth rate of this instability for a wave packet is sensitive to the presence of a background mean velocity (Bourget et al. 2014). Indeed, if the time scale of advection of the wave packet is faster than the growth rate of PSI, the instability may not have time to significantly distort the wave. Though this may play a role in our simulations, we believe that it is small. The waves are not spatially localized in the simulations; instead they fill the whole domain, partly due to the x periodicity. We note, however, that in the ocean where localized topographic features can generate localized wave packets, this effect could play a role, in particular for the longer low-mode internal tides. Instead, here we believe that the main reason for the behavior observed is the Doppler effect on the secondary waves.

Figure 5 clearly shows the distortion of the radiating waves by the mean current. The slope of internal tides changes: upstream waves have steeper slopes and downstream waves have gentle slopes. The wave rays are slanted due to Doppler effects. For a wave $\propto e^{i(kx-\omega_0 t)}$, the frequency in the frame moving with the fluid becomes $\omega_f = \omega_0 - U_{\mathrm{mc}}k$. For internal tides, the left-propagating waves have $k < 0$ since their horizontal group velocity is negative, and the right-propagating waves have $k > 0$ (positive horizontal group velocity). This implies that the left-propagating waves have a higher frequency $\omega_f = \omega_0 + U_{\mathrm{mc}}|k|$ and hence steeper slopes, while the right-propagating waves have lower frequencies $\omega_f = \omega_0 - U_{\mathrm{mc}}|k|$ and hence gentler slopes. The slopes shown in Fig. 5 change consistently with this theoretical prediction.

This can also be seen on the kinetic energy spectrum as a function of horizontal and vertical wavenumber (Fig. 7). The curves from linear theory accounting for Doppler shift are shown. (Note that the frequency of Doppler-shifted waves depends on the magnitude of the mean current but also on the horizontal wavenumber. Also note that their vertical wavenumber changes accordingly to satisfy the dispersion relation in the frame of the fluid.) The agreement with the numerical simulations suggests that the Doppler effect on the primary internal tides may be important.

These changes in the primary waves imply that the secondary waves generated in the moving frame via PSI have frequencies $(\omega_0 \pm U_{\mathrm{mc}}|k|)/2$. So the ''critical latitude'' at which these frequencies match the Coriolis frequency f will now be a function of the wavenumber. This may explain the widening of the latitude window for which tidal dissipation is enhanced in Fig. 4 with a mean current. We note also the generation of secondary waves at f and $\omega_f - f = \omega_0 + U_{\mathrm{mc}}|k| - f$ from the left-propagating wave ($k < 0$) in Fig. 7. For the right-propagating wave, those secondary waves are not generated since the frequency $\omega_f - f = \omega_0 - U_{\mathrm{mc}}|k| - f$ is below f.

Figure 8 illustrates schematically the Doppler effects on primary and secondary waves. Without mean current the primary wave at frequency ω_0 yields two secondary waves at frequency $\omega_0/2 = f$ at the critical latitude. With a mean current, in the frame of the fluid, the left-propagating wave can generate a secondary wave via PSI at frequency $(\omega_0 + U_{\mathrm{mc}}|k|)/2$, but the right-propagating wave cannot excite secondary waves at the critical latitude since the corresponding frequency $(\omega_0 - U_{\mathrm{mc}}|k|)/2$ is below f. So Doppler effects limit transfers from the primary wave and hence reduce the energy loss via PSI at the critical latitude.

This is also shown in Fig. 9, which schematically highlights the wavenumbers for which PSI cannot excite secondary waves [blue regions $\Leftrightarrow (\omega_0 - U_{\mathrm{mc}}k)/2 < f$]. The top panel shows the wave frequency in the frame of the fluid as a function of horizontal wavenumber with a mean current (oblique line $\omega_f = \omega_0 - U_{\mathrm{mc}}k$). The bottom diagram in Fig. 9 represents the energy of the waves from linear theory for $f = 0.53 \times 10^{-4}\,\mathrm{s}^{-1}$. In the presence of a mean current, primary waves with $k > k_c$ cannot exist since their frequency is below f (cross-hatching area) and the energy at those horizontal wavenumbers is lost through dissipation, but these represent a small amount of wave energy. The important

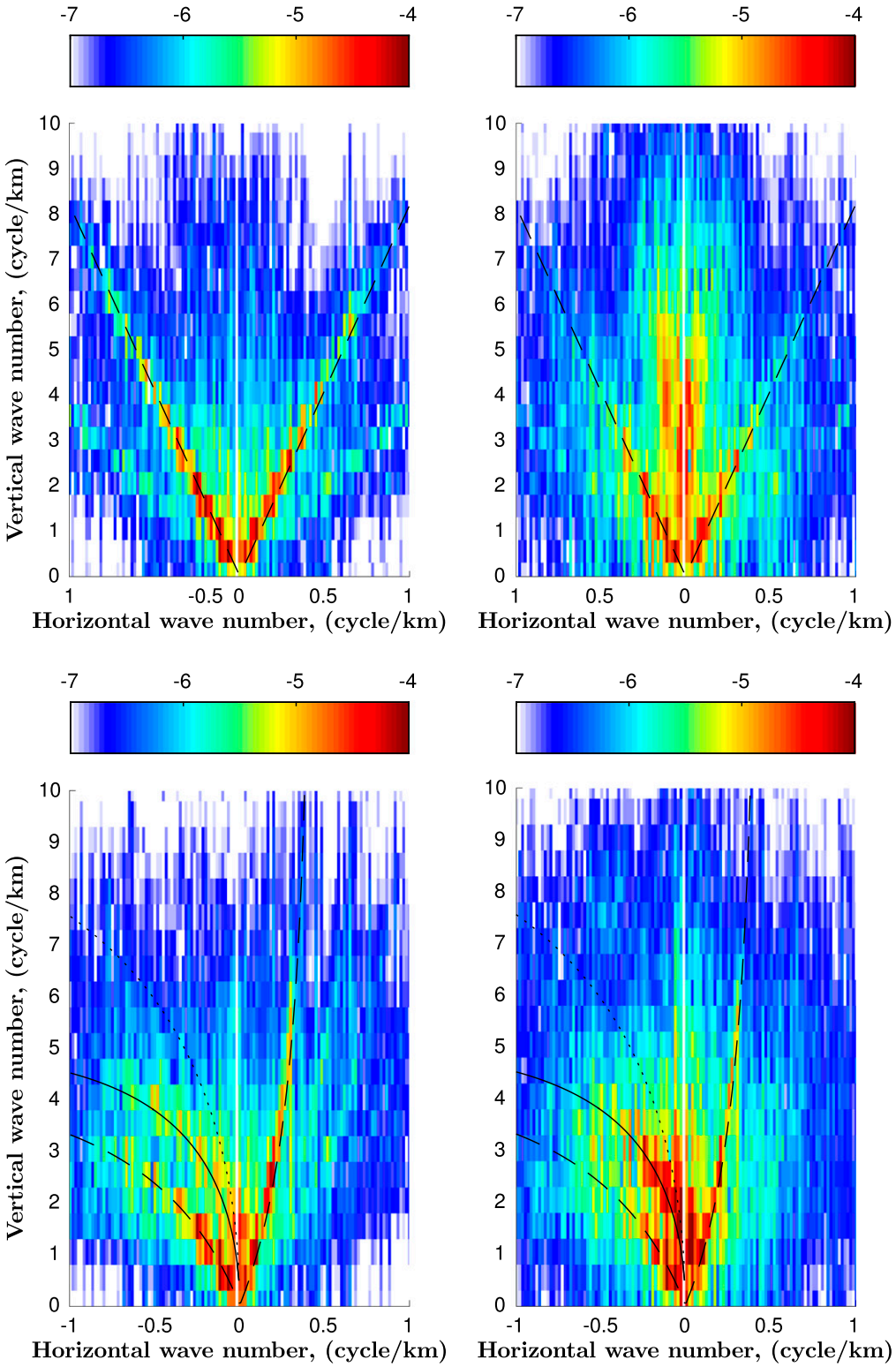

FIG. 7. Snapshots of the horizontal and vertical wavenumber kinetic energy spectrum from (top) simulation $f = 0.7 \times 10^{-4}\,\mathrm{s}^{-1}$ and $\alpha = 0$ and (bottom) simulation $f = 0.7 \times 10^{-4}\,\mathrm{s}^{-1}$ and $\alpha = 1$ after (left) 5 and (right) 19 days of simulation. The linear solution for the internal tide at fundamental frequency ω_0 is shown as black dashed lines (including Doppler effects with mean current bottom panels). In the bottom panels, the plain lines represent the Doppler-shifted wave at $\omega_f - f$ and the pointed line the Doppler-shifted wave at $\omega_f/2$.

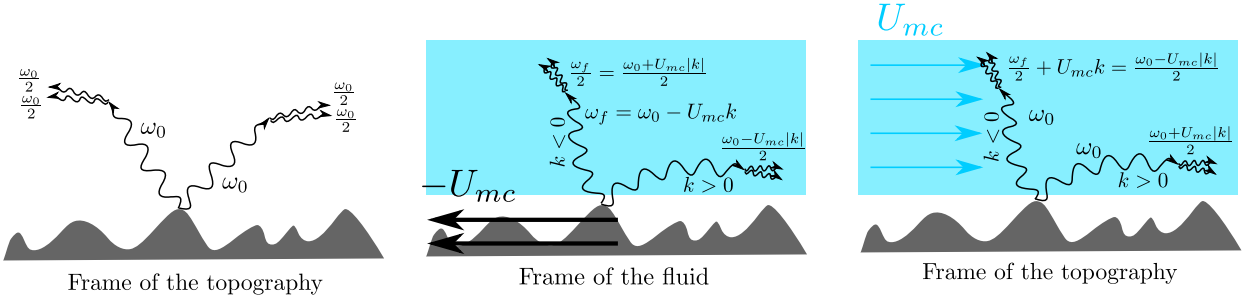

FIG. 8. Diagrams of the Doppler effect. The left diagram represents PSI without mean current in the frame of the topography. The middle diagram represents PSI with Doppler effect in the frame of the mean current U_{mc}. The right diagram represents the frequency of the waves in the frame of topography.

point is that waves with $k > k_c'$ (blue area) cannot generate secondary waves via PSI and hence propagate without losing energy.

To illustrate this effect more clearly, we turn to a simpler monochromatic topography. Indeed, the realistic topography used here has a wide range of horizontal wavenumbers, which makes it difficult to highlight the Doppler effect. We perform new simulations with a sinusoidal topography, thus containing only one horizontal wavenumber.

4. Results: Sinusoidal topography

The internal tides generated by sinusoidal topography $h(x) = h_0 \sin(k_t x)$ at the critical latitude are shown in Fig. 10 without mean current and in Fig. 11 with mean current. The topographic height h_0 and wavenumber k_t are chosen to match the horizontal and vertical Froude numbers of the realistic topography of the previous section, so that we remain in the same flow regimes and can expect similar behavior (see section 2 for detail). Two snapshots of the wave zonal velocity at 5 (middle) and 19 (right) days are shown in Figs. 10 and 11.

Without mean current, PSI yields strong inertial waves that are fully developed at day 19 (horizontal waves similar to the ones that were observed in Fig. 2). With mean current, the strong horizontal inertial waves are absent even at day 19. The transfer of energy to smaller scales via PSI is largely suppressed, consistent with the results from the previous section. We note though that the left-propagating waves still undergo some nonlinear transfer (as in the previous section; Fig. 7) to lower-frequency waves at f and $\omega_f - f$, yielding some waves with lower frequency (smaller slopes) at day 19. But the right-propagating wave is preserved even after 19 days, consistent with the theoretical prediction that Doppler effects prevent the generation of secondary waves via PSI for the right-propagating wave. Indeed, its frequency in the frame of the fluid is $\omega_f = \omega_0 - U_{mc} k_t$; hence, $\omega_f/2$ is below f at the critical latitude.

The vertical energy dissipation profiles at different latitudes are shown in Fig. 12. As before, blue curves

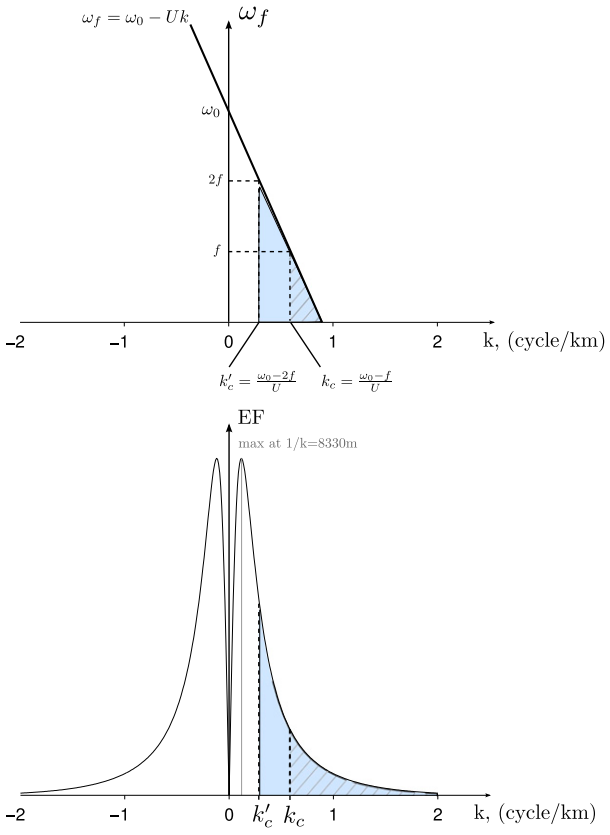

FIG. 9. Diagram of (top) frequency of the fluid ω_f as a function of the horizontal wavenumber k in case without mean current (horizontal line, $\omega_f = \omega_0$) and with mean current ($\omega_f = \omega_0 - U_{mc}k$). Diagram of (bottom) wave energy from linear theory as a function of the horizontal wavenumber k for the simulation with $f = 0.53 \times 10^{-4}$ and $\alpha = 0$. In the case of a mean current, the crosshatching section represents the domain where primary internal wave cannot exist ($\omega_0 - U_{mc}k \langle f \Leftrightarrow k \rangle k_c$). The blue area corresponds to the domain where PSI cannot exist and where waves propagate without dissipation [$(\omega_0 - Uk)/2 \langle f \Leftrightarrow k \rangle k_c'$].

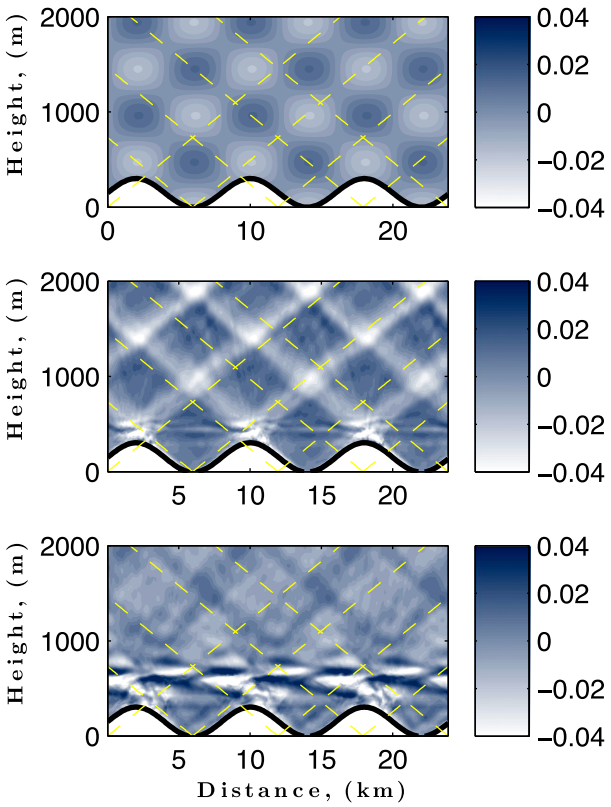

FIG. 10. Snapshots of the wave zonal velocity ($m\,s^{-1}$) from the simulation at the critical latitude with sinusoidal topography ($f = 0.7 \times 10^{-4}\,s^{-1}$, $\alpha = 0$), after (middle) 5 and (bottom) 19 days of simulation. (top) The linear solution is also shown for comparison as well as wave characteristics from the linear theory dispersion relation (dashed yellow lines).

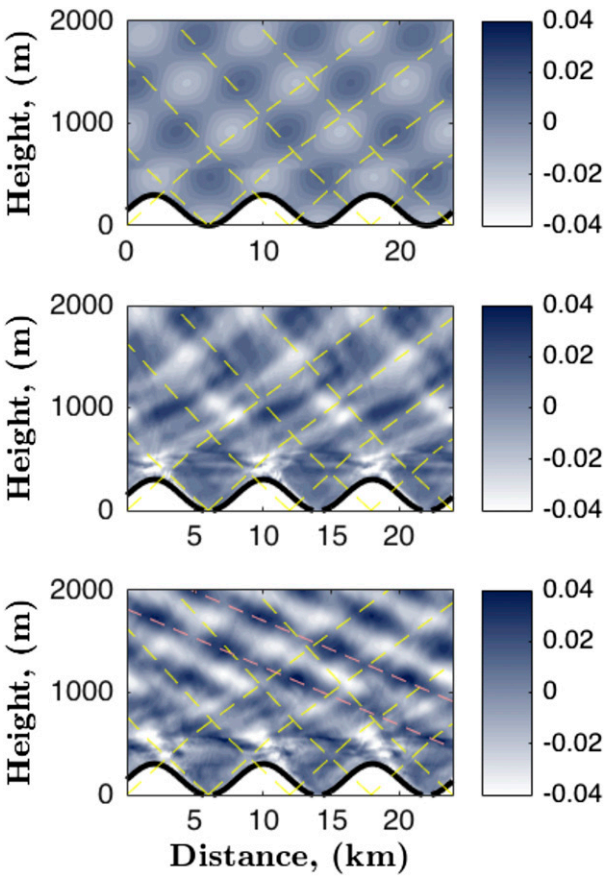

FIG. 11. As in Fig. 10, but for $\alpha = 1$. The coral dashed lines show the left-propagating secondary waves at $\omega_f - f$.

correspond to simulations without a mean current ($\alpha = 0$) and red curves correspond to simulations with a mean current ($\alpha = 1$). Without a mean current, we recover the critical latitude at $f = 0.7 \times 10^{-4}\,s^{-1}$, where the energy dissipation is enhanced in the first kilometer above topography. When a mean current is added, consistent with our earlier results, the profiles look similar regardless of the latitude.

The vertically integrated energy dissipation also confirms our earlier results (Fig. 13). As before, the energy dissipation in the bottom boundary layer does not depend on latitude, and without a mean current, the dissipation in the ocean interior peaks at the critical latitude $f \approx 0.7 \times 10^{-4}\,s^{-1}$. When a mean current is added, the maximum dissipation is weaker and more spread out with latitudes. In fact, we see two new critical latitudes emerging, where the energy dissipation is maximum ($f = 0.55 \times 10^{-4}\,s^{-1}$ and $f = 0.75 \times 10^{-4}\,s^{-1}$). In this simple case of monochromatic topography the interpretation of the results is clearer. Without mean current, the transfer of energy from the primary wave at ω_0 to secondary waves with frequency $\omega_0/2$ is maximum when $f = \omega_0/2$, that is, when the frequency of the secondary waves resonates with the Coriolis frequency. With mean current, the resonance occurs at two latitudes: $f = (\omega_0 - U_{mc}k_t)/2$ and $f = (\omega_0 + U_{mc}k_t)/2$. Those two critical latitudes hence correspond to frequencies of secondary waves with a Doppler shift.

Closer inspection shows that those two maxima are slightly asymmetric, with somewhat stronger dissipation at the higher latitude. Figure 14 shows wavenumber spectra of the kinetic energy for $f = 0.53 \times 10^{-4}\,s^{-1}$ and $f = 0.75 \times 10^{-4}\,s^{-1}$ at 5 (left) and 19 (right) days of simulation. At the beginning of the simulation, for both latitudes, spectra have energy localized at the unique topographic horizontal wavenumber k_t and its harmonics. After 19 days, there are new horizontal wavenumbers generated via nonlinearities. We can see again that there is a slight asymmetry between the two resonant latitudes. There is more energy at these new horizontal wavenumbers at $f = 0.75 \times 10^{-4}\,s^{-1}$, suggesting that the nonlinear transfer seems to be more vigorous at this latitude

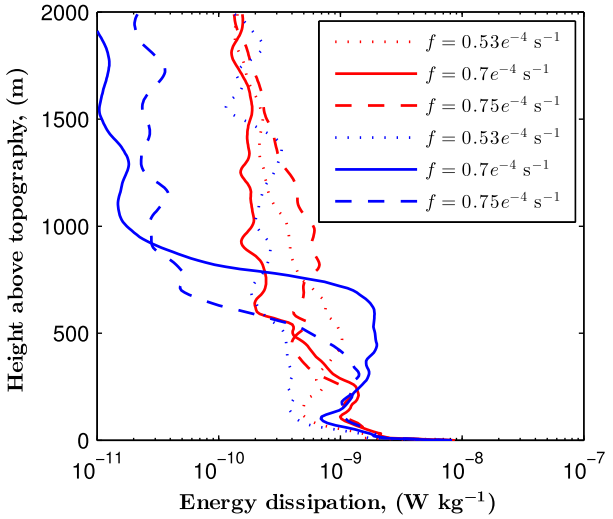

FIG. 12. Profiles of energy dissipation rates averaged zonally and over the last 10 days from simulations with sinusoidal topography. Blue profiles correspond to simulations with $\alpha = 0$, and red profiles correspond to simulations with $\alpha = 1$. The enhanced dissipation at the critical latitude without mean current disappears when a current is added, consistent with the earlier results for realistic topography.

(consistent with the dissipation in Fig. 13). We interpret this asymmetry as resulting from the slower group velocities of the waves at $f = 0.75 \times 10^{-4}\,\mathrm{s}^{-1}$, allowing nonlinearities to develop and to transfer a larger amount of energy to smaller scales.

5. Conclusions and discussion

In this paper, we investigate the latitudinal dependence of the local dissipation of internal tides near their generation site at the seafloor. We recover earlier results that were obtained in the idealized case of internal tides propagating in a quiescent ocean. In that case, without a mean current, the local dissipation of internal tides generated at rough topography is strongly enhanced at a critical latitude. The latter is the latitude where inertial waves at f resonate with the secondary waves generated by PSI at $\omega_0/2$. When a mean current is added, though weak (same order as the barotropic tide, a few centimeters per second), this behavior drastically changes. The dissipation peak at the critical latitude disappears and the local dissipation fraction of internal tides is closer to a constant, with two weak peaks at about 25° and 35° latitude.

Despite its simplicity, the idealized case of sinusoidal topography reproduces the main features of the internal tides generated by realistic multichromatic topography. This helps shed some light into the processes determining the latitudinal distribution of wave

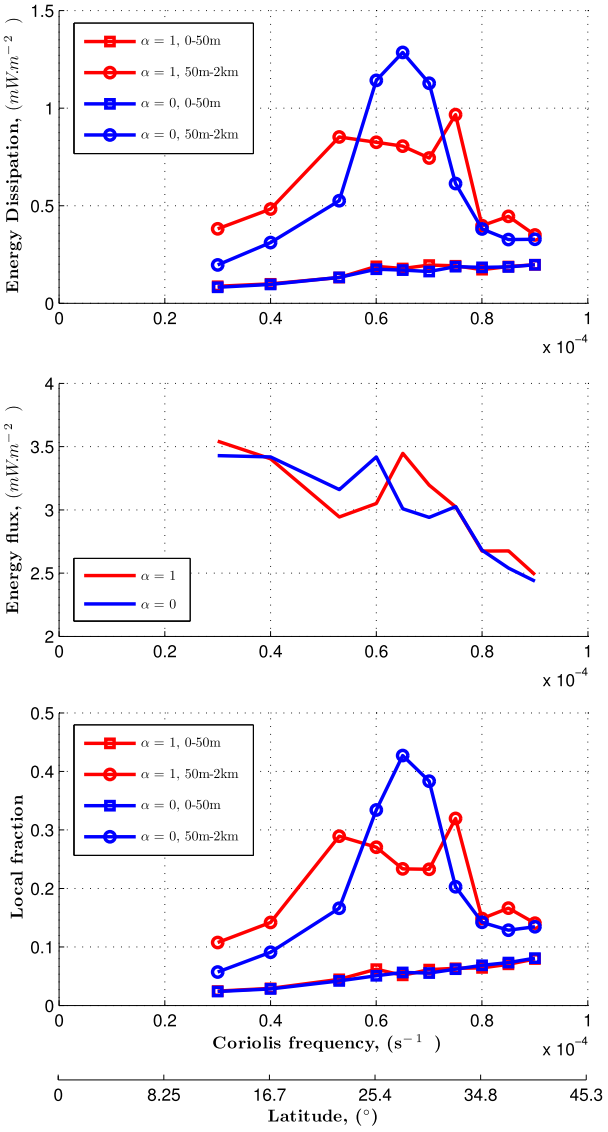

FIG. 13. (top) Energy dissipation rate integrated in the bottom 50 m (square) and between 50 and 2 km (circle) with sinusoidal topography. (middle) Energy flux at the topography. (bottom) Energy dissipation expressed as a fraction of the energy flux at the topography. Blue curves correspond to simulations with no U_{mc} and red curves correspond to simulations with U_{mc} and $\alpha = 1$. We recover the results of the previous section with realistic topography, namely, the dissipation enhancement at the critical latitude disappears when a mean current is added, and the dissipation is closer to a constant, with two new, weaker peaks at Doppler-shifted latitudes.

instability and dissipation. This sensitivity to a mean current can be understood by accounting for the Doppler shift of the primary internal tides as they propagate through the mean current. Different scales of the waves are shifted with different magnitudes, yielding a wide range of critical latitudes for the shifted primary frequency. In other words, the peak of

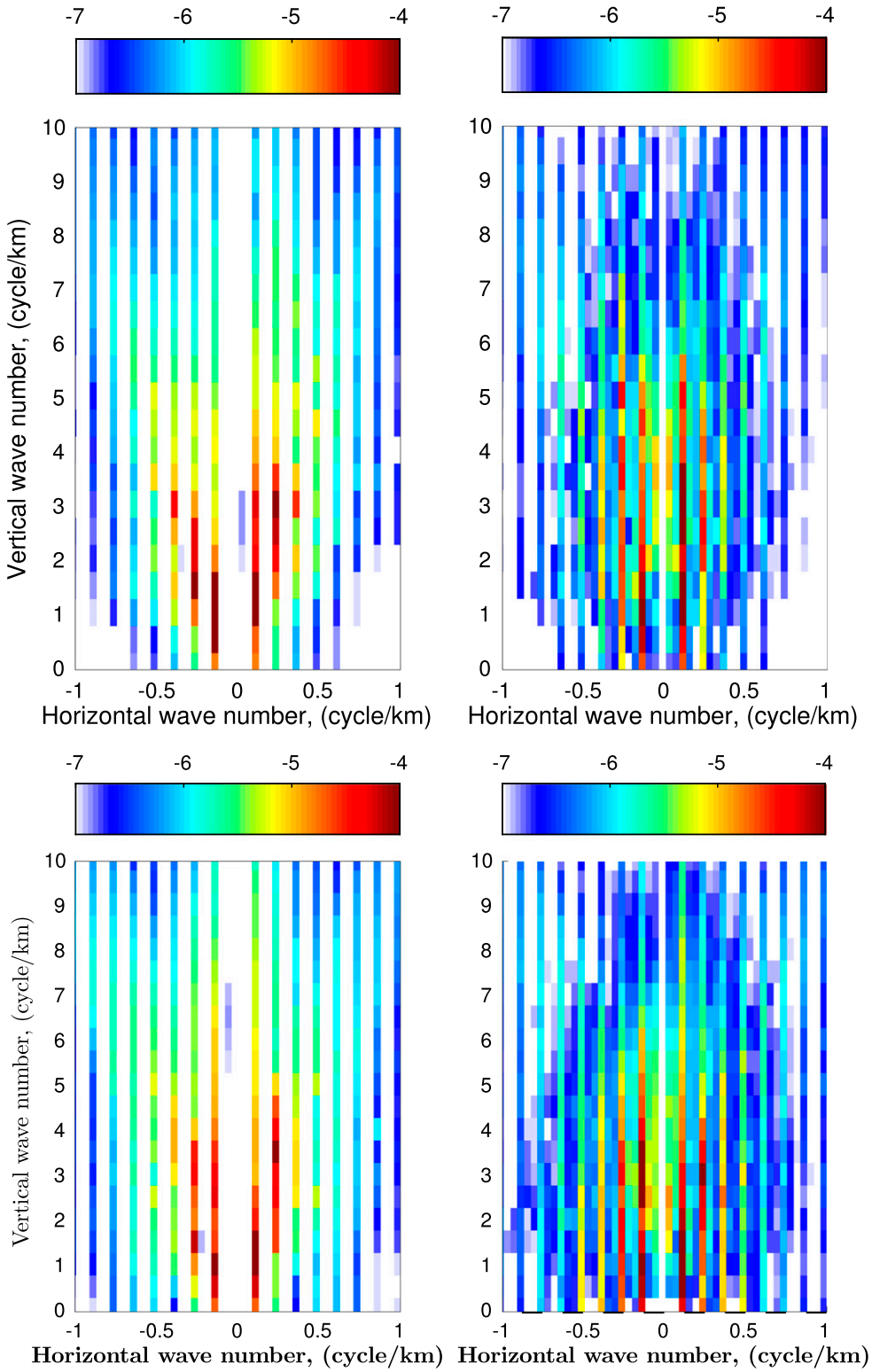

FIG. 14. Snapshots of the horizontal and vertical wavenumber spectrum from (top) simulation $f = 0.53 \times 10^{-4}\,\mathrm{s}^{-1}$ and $\alpha = 1$ and (bottom) simulation $f = 0.75 \times 10^{-4}\,\mathrm{s}^{-1}$ and $\alpha = 1$ after (left) 5 and (right) 19 days of simulation with sinusoidal topography.

dissipation at the critical latitude is not robust to the presence of a mean current.

This suggests that under realistic conditions, where waves are unlikely to propagate through a quiescent ocean, the local dissipation of the internal tide is not a strong function of latitude. The reduced dissipation fraction near the critical latitude implies that more wave energy than previously thought may propagate away from topography and hence may be available to dissipate in remote locations. A recent observational study also highlights the impact of Doppler effects on the propagation of near-inertial waves, which can propagate poleward beyond their critical latitude (Xie et al. 2016).

This has implications for the transformation of deep water masses and the abyssal circulation. Recent estimates of internal waves' impact on the overturning circulation point out the large uncertainty associated with remote dissipation of tides, which do not dissipate locally near their generation site. Depending on where this dissipation and the concomitant mixing occur, in particular its vertical structure, such mixing could drive 1 to 28 Sv of AABW upwelling. More work is desirable to help better constrain estimates of remote internal tide energy propagation and dissipation.

Acknowledgments. The authors thank Maxim Nikurashin for providing further details about the setting of the MITgcm simulations of Nikurashin and Legg (2011). C. M. gratefully acknowledges financial support from the Chair for Sustainable Development at Ecole Polytechnique. We acknowledge CINES/GENCI, France, for providing access and support to their computing platform JADE as well as the PRACE Research Infrastructure computing resource Curie based in France at TGCC. The authors thank the Direction Générale de l'Armement (DGA) for the financial support of Océane Richet's Ph.D. research.

APPENDIX

Mean Current

In this appendix, we show that adding a mean current to the simulations of internal tides does not impact significantly the generation of internal tides at the topography. Indeed, we want to investigate the impact of a mean current on the propagation and dissipation of waves, not on their generation.

To ensure minimal interaction of the mean current with topography, we start increasing the strength of the mean current near the highest topography peak. The amplitude of U_{mc} increases from 0 near the maximum height of topography to αU_{tide} a hundred meters above that height.

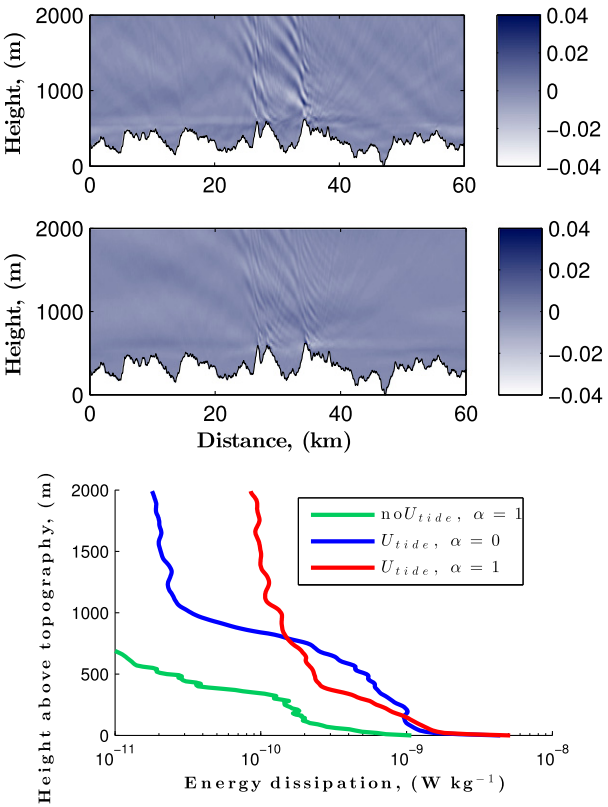

FIG. A1. Snapshots of the wave zonal velocity (m s^{-1}) from the simulation without a tidal flow ($f = 0.7 \times 10^{-4}$ s^{-1}, $\alpha = 1$ and $U_{\mathrm{tide}} = 0$ m s^{-1}) after (top) 5 and (middle) 19 days of simulation. (bottom) The vertical profile of energy dissipation averaged over the last 10 days of the simulation. For comparison, the vertical profiles with tidal forcing are repeated from Fig. 6.

In the simulations discussed in the paper, the shear layer starts at $z = 500$ m and ends at 600 m, above which the mean current is constant (Fig. 1). Here, we show that even if the shear layer is lowered between $z = 400$ and 500 m to accentuate the generation of lee waves by the mean current, the generation and the energy dissipation of those lee waves are negligible compared to the internal tides discussed in the paper. The mean current used in the paper (starting higher at 500 m) yields even weaker lee waves and dissipation.

Figure A1 (top and middle panels) shows snapshots of a simulation with mean current only (no barotropic tide). Some lee waves are generated at the highest topographic peaks, but the signal is very weak compared to the internal tides shown in Figs. 2 or 5. The energy dissipation associated to those lee waves is small compared to the energy dissipation associated with internal tides (Fig. A1, bottom panel). We are therefore

confident that the presence of lee waves does not impact the results presented here.

REFERENCES

Alford, M. H., J. A. MacKinnon, Z. Zhao, R. Pinkel, J. Klymak, and T. Peacock, 2007: Internal waves across the Pacific. *Geophys. Res. Lett.*, **34**, L24601, doi:10.1029/2007GL031566.

Bell, T. H., 1975: Lee waves in stratified flows with simple harmonic time dependence. *J. Fluid Mech.*, **67**, 705–722, doi:10.1017/S0022112075000560.

Booker, J. R., and F. P. Bretherton, 1967: The critical layer for internal gravity waves in a shear flow. *J. Fluid Mech.*, **27**, 513–539, doi:10.1017/S0022112067000515.

Bourget, B., T. Dauxois, S. Joubaud, and P. Odier, 2013: Experimental study of parametric subharmonic instability for internal plane waves. *J. Fluid Mech.*, **723**, 1–20, doi:10.1017/jfm.2013.78.

——, H. Scolan, T. Dauxois, M. Le Bars, P. Odier, and S. Joubaud, 2014: Finite-size effects in parametric subharmonic instability. *J. Fluid Mech.*, **759**, 739–750, doi:10.1017/jfm.2014.550.

Bouruet-Aubertot, P., J. Sommeria, and C. Staquet, 1995: Breaking of standing internal gravity waves through two-dimensional instabilities. *J. Fluid Mech.*, **285**, 265–301, doi:10.1017/S0022112095000541.

De Lavergne, C., G. Madec, J. Le Sommer, A. J. G. Nurser, and A. C. Naveira Garabato, 2016a: On the consumption of Antarctic Bottom Water in the abyssal ocean. *J. Phys. Oceanogr.*, **46**, 635–661, doi:10.1175/JPO-D-14-0201.1.

——, ——, ——, ——, and ——, 2016b: The impact of a variable mixing efficiency on the abyssal overturning. *J. Phys. Oceanogr.*, **46**, 663–681, doi:10.1175/JPO-D-14-0259.1.

Ferrari, R., 2014: What goes down must come up. *Nature*, **513**, 179–180, doi:10.1038/513179a.

——, M. F. Jansen, J. F. Adkins, A. Burke, A. L. Stewart, and A. F. Thompson, 2014: Antarctic sea ice control on ocean circulation in present and glacial climates. *Proc. Natl. Acad. Sci. USA*, **111**, 8753–8758, doi:10.1073/pnas.1323922111.

Garrett, C., and W. Munk, 1979: Internal waves in the ocean. *Annu. Rev. Fluid Mech.*, **11**, 339–369, doi:10.1146/annurev.fl.11.010179.002011.

——, and E. Kunze, 2007: Internal tide generation in the deep ocean. *Annu. Rev. Fluid Mech.*, **39**, 57–87, doi:10.1146/annurev.fluid.39.050905.110227.

Gemmrich, J., and J. M. Klymak, 2015: Dissipation of internal wave energy generated on a critical slope. *J. Phys. Oceanogr.*, **45**, 2221–2238, doi:10.1175/JPO-D-14-0236.1.

Gerkema, T., 2001: Internal and interfacial tides: Beam scattering and local generation of solitary waves. *J. Mar. Res.*, **59**, 227–255, doi:10.1357/002224001762882646.

Goff, J. A., and T. H. Jordan, 1989: Stochastic modeling of seafloor morphology: A parameterized Gaussian model. *Geophys. Res. Lett.*, **16**, 45–48, doi:10.1029/GL016i001p00045.

——, and B. K. Arbic, 2010: Global prediction of abyssal hill roughness statistics for use in ocean models from digital maps of paleo-spreading rate, paleo-ridge orientation, and sediment thickness. *Ocean Modell.*, **32**, 36–43, doi:10.1016/j.ocemod.2009.10.001.

Hazewinkel, J., and K. Winters, 2011: PSI of the internal tide on a β plane: Flux divergence and near-inertial wave propagation. *J. Phys. Oceanogr.*, **41**, 1673–1682, doi:10.1175/2011JPO4605.1.

Jayne, S. R., 2009: The impact of abyssal mixing parameterizations in an ocean general circulation model. *J. Phys. Oceanogr.*, **39**, 1756–1775, doi:10.1175/2009JPO4085.1.

Ledwell, J., E. Montgomery, K. Polzin, L. S. Laurent, R. Schmitt, and J. Toole, 2000: Evidence for enhanced mixing over rough topography in the abyssal ocean. *Nature*, **403**, 179–182, doi:10.1038/35003164.

Lefauve, A., C. Muller, and A. Melet, 2015: A three-dimensional map of tidal dissipation over abyssal hills. *J. Geophys. Res. Oceans*, **120**, 4760–4777, doi:10.1002/2014JC010598.

MacKinnon, J. A., and K. B. Winters, 2005: Subtropical catastrophe: Significant loss of low-mode tidal energy at 28.9°. *Geophys. Res. Lett.*, **32**, L15605, doi:10.1029/2005GL023376.

——, M. H. Alford, O. Sun, R. Pinkel, Z. Zhao, and J. Klymak, 2013: Parametric subharmonic instability of the internal tide at 29°N. *J. Phys. Oceanogr.*, **43**, 17–28, doi:10.1175/JPO-D-11-0108.1.

Marshall, J., A. Adcroft, C. Hill, L. Perelman, and C. Heisey, 1997: A finite-volume, incompressible Navier Stokes model for studies of the ocean on parallel computers. *J. Geophys. Res.*, **102**, 5753–5766, doi:10.1029/96JC02775.

Mashayek, A., R. Ferrari, M. Nikurashin, and W. R. Peltier, 2015: Influence of enhanced abyssal diapycnal mixing on stratification and the ocean overturning circulation. *J. Phys. Oceanogr.*, **45**, 2580–2597, doi:10.1175/JPO-D-15-0039.1.

Maslowe, S., 1986: Critical layers in shear flows. *Annu. Rev. Fluid Mech.*, **18**, 405–432, doi:10.1146/annurev.fl.18.010186.002201.

Melet, A., S. Legg, and R. Hallberg, 2016: Climatic impact of parameterized local and remote tidal mixing. *J. Climate*, **29**, 3473–3500, doi:10.1175/JCLI-D-15-0153.1.

Muller, C. J., and O. Bühler, 2009: Saturation of the internal tides and induced mixing in the abyssal ocean. *J. Phys. Oceanogr.*, **39**, 2077–2096, doi:10.1175/2009JPO4141.1.

Müller, P., and N. Xu, 1992: Scattering of oceanic internal gravity waves off random bottom topography. *J. Phys. Oceanogr.*, **22**, 474–488, doi:10.1175/1520-0485(1992)022<0474:SOOIGW>2.0.CO;2.

Munday, D. R., L. C. Allison, H. L. Johnson, and D. P. Marshall, 2011: Remote forcing of the Antarctic Circumpolar Current by diapycnal mixing. *Geophys. Res. Lett.*, **38**, L08609, doi:10.1029/2011GL046849.

Nikurashin, M., and R. Ferrari, 2011: Global energy conversion rate from geostrophic flows into internal lee waves in the deep ocean. *Geophys. Res. Lett.*, **38**, L08610, doi:10.1029/2011GL046576.

——, and S. Legg, 2011: A mechanism for local dissipation of internal tides generated at rough topography. *J. Phys. Oceanogr.*, **41**, 378–395, doi:10.1175/2010JPO4522.1.

——, and R. Ferrari, 2013: Overturning circulation driven by breaking internal waves in the deep ocean. *Geophys. Res. Lett.*, **40**, 3133–3137, doi:10.1002/grl.50542.

——, G. K. Vallis, and A. Adcroft, 2012: Routes to energy dissipation for geostrophic flows in the Southern Ocean. *Nat. Geosci.*, **6**, 48–51, doi:10.1038/ngeo1657.

Polzin, K. L., 2009: An abyssal recipe. *Ocean Modell.*, **30**, 298–309, doi:10.1016/j.ocemod.2009.07.006.

——, J. Toole, J. Ledwell, and R. Schmitt, 1997: Spatial variability of turbulent mixing in the abyssal ocean. *Science*, **276**, 93–96, doi:10.1126/science.276.5309.93.

Rainville, L., and R. Pinkel, 2006: Propagation of low-mode internal waves through the ocean. *J. Phys. Oceanogr.*, **36**, 1220–1236, doi:10.1175/JPO2889.1.

Samelson, R. M., 1998: Large-scale circulation with locally enhanced vertical mixing. *J. Phys. Oceanogr.*, **28**, 712–726, doi:10.1175/1520-0485(1998)028<0712:LSCWLE>2.0.CO;2.

Staquet, C., and J. Sommeria, 2002: Internal gravity waves: From instabilities to turbulence. *Annu. Rev. Fluid Mech.*, **34**, 559–593, doi:10.1146/annurev.fluid.34.090601.130953.

St. Laurent, L., and C. Garrett, 2002: The role of internal tides in mixing the deep ocean. *J. Phys. Oceanogr.*, **32**, 2882–2899, doi:10.1175/1520-0485(2002)032<2882:TROITI>2.0.CO;2.

Talley, L. D., 2013: Closure of the global overturning circulation through the Indian, Pacific, and Southern Oceans: Schematics and transports. *Oceanography*, **26**, 80–97, doi:10.5670/oceanog.2013.07.

Waterhouse, A. F., and Coauthors, 2014: Global patterns of diapycnal mixing from measurements of the turbulent dissipation rate. *J. Phys. Oceanogr.*, **44**, 1854–1872, doi:10.1175/JPO-D-13-0104.1.

Xie, X., Q. Liu, X. Shang, G. Chen, and D. Wang, 2016: Poleward propagation of parametric subharmonic instability-induced inertial waves. *J. Geophys. Res. Oceans*, **121**, 1881–1895, doi:10.1002/2015JC011194.